

# OpenLiDARMap: Zero-Drift Point Cloud Mapping using Map Priors

Dominik Kulmer<sup>1</sup>, Maximilian Leitenstern<sup>1</sup>, Marcel Weinmann<sup>1</sup> and Markus Lienkamp<sup>1</sup>

**Abstract**— Accurate localization is a critical component of mobile autonomous systems, especially in Global Navigation Satellite Systems (GNSS)-denied environments where traditional methods fail. In such scenarios, environmental sensing is essential for reliable operation. However, approaches such as LiDAR odometry and Simultaneous Localization and Mapping (SLAM) suffer from drift over long distances, especially in the absence of loop closures. Map-based localization offers a robust alternative, but the challenge lies in creating and georeferencing maps without GNSS support. To address this issue, we propose a method for creating georeferenced maps without GNSS by using publicly available data, such as building footprints and surface models derived from sparse aerial scans. Our approach integrates these data with onboard LiDAR scans to produce dense, accurate, georeferenced 3D point cloud maps. By combining an Iterative Closest Point (ICP) scan-to-scan and scan-to-map matching strategy, we achieve high local consistency without suffering from long-term drift. Thus, we eliminate the reliance on GNSS for the creation of georeferenced maps. The results demonstrate that LiDAR-only mapping can produce accurate georeferenced point cloud maps when augmented with existing map priors.

## I. INTRODUCTION

Localization is essential for mobile autonomous systems, enabling them to navigate and interact with their environment effectively. In recent years, significant advancements have been made in LiDAR odometry [1], [2], LiDAR-inertial odometry [3]–[5], and Simultaneous Localization and Mapping (SLAM) [6]–[9]. Despite their advances, these methods remain prone to drift, especially during long-term operations. While loop closure can help reduce drift by aligning the current position with a previously visited location, it does not guarantee an accurate reconstruction of the intermediate path. Additionally, loops are not always present, especially in linear or open-ended trajectories.

Map-based localization offers an alternative by using pre-existing maps to constrain localization and eliminate drift. However, these algorithms rely on the availability of maps, which limits their applicability in unknown environments where LiDAR odometry, LiDAR-inertial odometry, and SLAM excel. OpenStreetMap<sup>1</sup> (OSM), a globally available web-based platform, provides maps that can be used for localization with minimal geographic constraints. However, these standard-definition (SD) maps cannot support high-precision localization due to their limited accuracy.

<sup>1</sup>Dominik Kulmer, Ilir Tahiraj, and Markus Lienkamp are with the Institute of Automotive Technology, Munich Institute of Robotics and Machine Intelligence (MIRMI), Technical University of Munich, 85748 Garching, Germany

Corresponding author: dominik.kulmer@tum.de

<sup>1</sup>www.openstreetmap.org

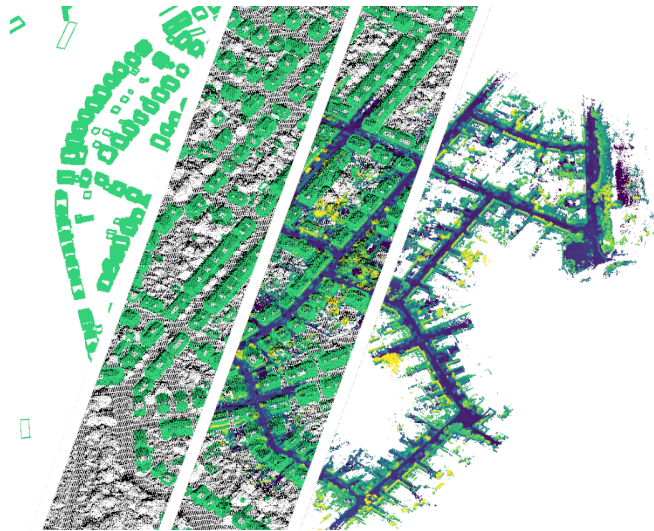


Fig. 1: Representation of the different map priors and formats from the building approximations on the left to the final georeferenced point cloud map on the right for KITTI Seq. 00.

High-definition (HD) maps represent the environment at a resolution of 10 cm to 20 cm [10] and are ideal for precise localization [11], [12]. These maps typically consist of high accuracy point cloud maps. However, the map generation process suffers from the same drift and accuracy issues as the localization itself. Global Navigation Satellite Systems (GNSS) offer a global reference to mitigate drift and enable georeferenced mapping. However, their signals are highly susceptible to degradation in obstructed environments. This vulnerability significantly reduces their reliability for producing high-precision maps.

This work addresses these challenges by proposing a method for high-definition map generation that combines publicly available building maps and surface models with onboard LiDAR data. By leveraging these resources, the approach eliminates reliance on GNSS and enables the creation of accurate, georeferenced point cloud maps (Figure 1).

The main contribution of this paper is a pose-graph-based optimization algorithm that combines Iterative Closest Point (ICP) scan-to-scan with scan-to-map matching of publicly available building data and sparse surface models to generate accurate georeferenced point cloud maps without the need for GNSS data. While scan-to-map matching regulates long-term drift, scan-to-scan matching maintains local consistency between individual LiDAR scans. It also enables the approach to compensate for missing buildings and outdated map data

or to bridge short areas not present on the sparse prior map.

Our approach uses neither learning-based methods, feature extraction techniques, nor loop closures. We show that the approach works with a single parameter set on different platforms, like vehicles and segways, with different LiDAR setups, ranging from a single 32-channel LiDAR to a modern multi-LiDAR setup, and in various environments, such as residential and rural regions.

In sum, we make four claims: Our approach is able to (I) map long sequences without accumulating drift over time; (II) automatically georeference the generated map without GNSS data; (III) keep a high local consistency of the generated map; (IV) yield promising results on multiple robotic platforms, LiDAR setups and environments without further tuning.

To build on our work, we provide an open source implementation upon acceptance of the paper.

## II. RELATED WORK

When available, high-precision RTK-GNSS signals are often used for georeferenced mapping, requiring precise time synchronization between sensors and optimal signal reception along the mapped route. However, GNSS signal interruptions, such as in urban canyons or underpasses, pose a challenge to continuous mapping. Hybrid pipelines have been proposed to deal with signal interruption. These typically involve creating an initial map using LiDAR odometry or SLAM, followed by post-processing to georeference the map using GNSS data [13]. While this approach can bridge short gaps without GNSS, it remains dependent on intermittent signal availability. SLAM techniques fused with GNSS signals can also produce georeferenced maps [11], [14], [15], but require careful tuning of sensor weights and suffer from the same dependency on GNSS signal quality.

OSM represents an alternative to GNSS for global localization and mapping, relying on widely available crowd-sourced map data. [16] improved global localization accuracy by combining visual odometry with Monte Carlo localization, using chamfer matching to align trajectories with OSM maps. [17] proposed a probabilistic navigation method that aligns 3D-LiDAR sensor data with OSM tracks using semantic terrain information and a Markov-Chain Monte Carlo framework. [18] introduced a Gaussian-Gaussian cloud model for visual odometry, where OSM road constraints help mitigate drift and resolve scale ambiguities. [19] used OSM to create orthophoto-style images of roads and building footprints and generated semantic descriptors to match LiDAR data. [20] introduced a localization method that detects building facades using stereo image-based point clouds and matches them with 3D building models from OSM. Similarly, [21] computed angular distances to buildings within OSM and produced descriptors that match LiDAR data to achieve localization. [22] used a particle filter to integrate LiDAR point clouds with OSM constraints such as road boundaries, improving accuracy by exploiting map geometry. [23] extended this concept by combining SLAM

with OSM priors, integrating 2D building geometry into trajectory estimation through LiDAR scan matching.

These methods highlight the diverse applications of OSM in reducing drift for mapping and localization in the absence of GNSS signals. However, challenges such as limited accuracy and dependence on map accuracy remain.

Satellite or aerial imagery is another alternative for georeferenced mapping by aligning ground-level observations with overhead map features. [24] presented a cross-view localization framework that leverages semantic LiDAR point clouds alongside top-down RGB satellite imagery for georeferenced mapping. Similarly, [25] refined cross-view localization techniques to operate effectively in areas lacking fine-grained ground truth, relying on coarse satellite or map data to improve accuracy. However, the inherent misalignment between ground observations and aerial imagery remains a persistent challenge, often resulting in significant localization errors.

Pure LiDAR odometry and SLAM methods lack georeferencing, while GNSS-based approaches remain vulnerable to environmental interference and signal loss. OSM-based methods, while independent of GNSS, rely on the accuracy of crowd-sourced maps that may be outdated or inaccurate. Satellite data provides broad coverage but often suffers from alignment problems between ground and aerial imagery.

These limitations highlight the need for novel approaches that can achieve georeferenced mapping without relying on GNSS.

## III. GEOREFENCED POINT CLOUD MAPPING

In this section, we explain our LiDAR-based point cloud mapping approach. The main idea is to combine scan-to-scan matching with scan-to-map matching of reference maps of publicly available building information and sparse surface models in a pose-graph optimization framework. The advantage of our method is that we maintain high local consistency while eliminating long-term drift without the need for additional sensors. Our mapping procedure can be summarized in five steps (Figure 3); while the first one is done beforehand, the others are performed for each input frame:

- 1) Generating a sparse reference point cloud map from openly available building data and surface models.
- 2) Scan matching of the current LiDAR scan and the sparse reference map.
- 3) Scan matching of the current LiDAR scan and a local submap of previous LiDAR scans.
- 4) Performing a graph optimization of the resulting poses.
- 5) Estimating the initial guess for the next LiDAR scan from a constant distance and rotation assumption.

### A. Generating Sparse Reference Maps

OSM provides, besides road infrastructure data, building outlines for much of the world. In addition to geometric outlines, OSM can store semantic attributes such as building height or number of stories. Beyond OSM, other publicly available local data sources, such as Germany's open data

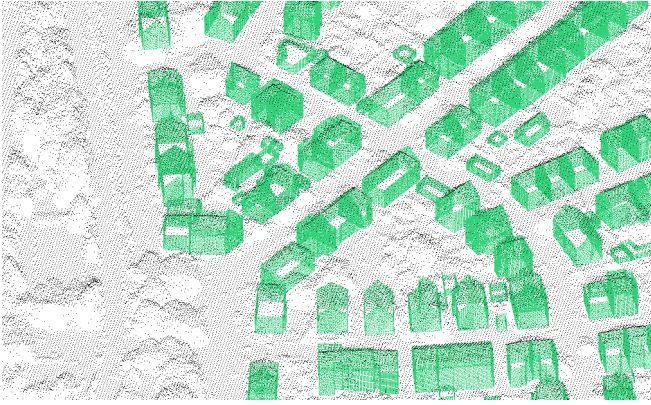


Fig. 2: Exemplary illustration of a combined sparse point cloud map of (green) approximated building data and (black) the surface model with a ground sampling distance of 1 m around the starting position of KITTI Seq. 00.

portal<sup>2</sup>, provide detailed building information. From this data, sparse georeferenced three-dimensional point clouds can be generated. Depending on data availability, a simplified building representation is derived from OSM data or more sophisticated building models, such as those from the German open data portal. While building models can directly be approximated as a point cloud due to their inherent spatial representation, OSM data requires an estimation for building heights. We assume a height of 4 m per floor, with a default height of 8 m for untagged buildings. The resulting point cloud approximates the building shape using a tessellation with an edge length of 0.5 m.

In addition to building data, three-dimensional surface measurements are available for many regions of the world<sup>2,3,4,5</sup>. These surface measurements are typically provided as either surface models or elevation models with varying ground sampling distances, often in the region of 1 m to 5 m. Surface models capture raw LiDAR scans or a downsampled subset, while elevation models represent the terrain alone, excluding vegetation and structures. This data is just another representation of point clouds. Therefore, it can be combined with the building point cloud data to create a sparse georeferenced point cloud map (Figure 2). We use this map as a reference in the following scan-to-map matching.

### B. Scan-to-Map Matching

Our approach is based on *small\_gicp* [26], a lightweight, header-only C++ library designed for point cloud preprocessing and scan matching. We adopt a voxel hash map as our data structure to efficiently handle large point clouds, allowing fast nearest-neighbor searches. The data within each voxel is stored according to the linear iVox principle [3].

The current input frame is pre-processed with a voxel-based downsampling before the scan matching. The parameters for our entire processing chain can be taken from subsection III-F.

A manual initial pose estimate on the map is provided for the first input frame and subsequently refined through scan-to-map matching. For subsequent frames, the initial estimate is derived from the results of the pose-graph optimization, as described in subsection III-E. The scan matching process uses the ICP algorithm for its simplicity and robustness. Outliers are managed using the Geman-McClure robust kernel, and the optimization is carried out using the Gauss-Newton method. The scan matching process returns a global pose within our reference map.

### C. Scan-to-Scan Matching

The same procedure used for scan-to-map matching is applied to scan-to-scan matching, using the same preprocessing, data structure, and optimization.

For scan-to-scan matching, a local submap of the environment is incrementally constructed. The first input frame serves as the registration target for the subsequent scan frame. If the relative transformation between consecutive frames is below 0.1 m, the system assumes a static state. Therefore, no pose is provided for the optimization, and the optimization process for both scan-to-scan and scan-to-map matching is skipped. In dynamic scenarios, as defined by this threshold, the scan-to-scan matching outputs the relative transformation.

After the pose-graph optimization, the current frame is integrated into the local submap using the determined transformation. To maintain a local representation of the environment, any voxels in the submap that are more than 100 m from the current position are removed. From the second frame onward, scan matching is performed against this evolving local submap rather than solely against the previous frame. This approach is inspired by KISS-ICP [1] and leverages the initial pose estimation described in subsection III-E.

### D. Pose-Graph Optimization

Our approach integrates scan-to-scan and scan-to-map matching into an optimization framework using the Ceres solver [27]. The optimization problem is formulated as a non-linear least squares problem (Equation 1), where residuals are minimized to align the current pose estimate with the scan matching results.

$$\min_x \frac{1}{2} \sum_i \rho_i (\|f_i(x_{i_1}, \dots, x_{i_k})\|^2) \quad (1)$$

$\rho_i$  represents a loss function to reduce the influence of outliers on the solution.  $f_i(\cdot)$  is the cost function, which depends on the parameter block  $(x_{i_1}, \dots, x_{i_k})$ .

Unlike batch optimization methods, which process all frames simultaneously, the proposed approach employs frame-by-frame optimization. For each frame, the residuals are computed as the deviation between the initial pose

<sup>2</sup>www.govdata.de

<sup>3</sup>www.data.europa.eu

<sup>4</sup>www.data.gov.uk

<sup>5</sup>www.usgs.gov







For the nearest neighbor search, we consider 27 neighboring voxels within a  $3 \times 3 \times 3$  cube around the query point. A correspondence threshold of 6 m is applied to filter out invalid associations during scan matching. For all robust kernels used in the optimization process, we use a static kernel width of 1.0 to ensure consistent outlier handling throughout the pipeline.

#### IV. EXPERIMENTAL EVALUATION

We present our experiments to show the capabilities of our method. The results of our experiments support our key claims, namely that we can (I) map long sequences without accumulating drift over time; (II) automatically georeference the generated map without GNSS data; (III) keep a high local consistency of the generated map; (IV) yield promising results on multiple robotic platforms, LiDAR setups and environments without further tuning.

##### A. Experimental Setup

We evaluate our method on the three different long-distance datasets KITTI Seq. 00 [28], [29], NCLT 2013-01-10 [30], and EDGAR Campus, each using different robot platforms and sensor setups. The characteristics can be found in Table I. The KITTI dataset is a widely accepted benchmark for evaluating localization and mapping algorithms. Following the approach demonstrated by IMLS-SLAM [31] and later adopted by others, such as KISS-ICP [1] and CT-ICP [6], we apply a correction to the intrinsic calibrations around the vertical axis. Specifically, the point clouds are adjusted by an angle of  $0.375^\circ$  to ensure accurate alignment.

The NCLT dataset employs a Segway platform, introducing significant challenges due to the vehicle’s high dynamics and diverse environmental conditions. The dataset encompasses outdoor scenes ranging from wide-open parking areas to narrow building passages.

The EDGAR dataset is the longest of the three tested datasets and covers the Technical University of Munich campus in Garching, Germany. It includes a variety of environments, from building complexes and extensive parking areas to country roads, with vehicle speeds ranging from low speeds up to  $70 \text{ km h}^{-1}$ . The route traverses both dense and sparsely built-up areas. Unlike KITTI and NCLT, EDGAR features a multi-LiDAR setup, consisting of two spinning and two solid-state LiDARs, which enhances data richness and coverage. While the first two datasets are freely available, the EDGAR Campus dataset is proprietary. Information about the sensor setup can be found in [32], [33].

All vehicles are equipped with RTK-GNSS systems to provide the ground truth data.

The quality of the maps created cannot be answered with a single metric. A distinction is made between global deviations, such as drift, and local inconsistencies.

##### B. Global Displacement Evaluation

We evaluate our approach using the Absolute Trajectory Error (ATE) and the KITTI metric for the Relative Trajectory Error (RTE). The KITTI metric samples the trajectory into

TABLE I: Characteristic of the datasets used for the evaluation.

Dataset	Length [m]	Frames [#]	Sensor Setup	Scenario
KITTI Seq. 00	3724	4541	Velodyne HDL-64	outdoor, residential, car
NCLT 2013-01-1	1311	5120	Velodyne HDL-32E	outdoor/indoor, residential, segway
EDGAR Campus	5289	9104	2x Ouster OS1-128 2x Seyond Falcon	outdoor, rural/residential, car

segments of varying lengths, ranging from 100 m to 800 m, and calculates the average relative translational and rotational errors. While the ATE measures the global deviation of the estimated trajectory from the ground truth, the KITTI metric provides insights into the accuracy over medium-length segment pieces.

We compare our approach with three OSM-based global localization and mapping methods and a satellite imagery-based approach for the ATE evaluation. Additionally, we include KISS-ICP as a LiDAR odometry baseline for comparison. However, open-source code is unavailable for all three of the OSM-based methods, and the repository for the imagery-based method is outdated. As a result, we rely on the published data from their respective published works. To enable a comparison with the ground truth, which is positioned in a local coordinate system originating in the first frame, we transform our georeferenced results into the first frame to obtain the same local representation. Then, we calculate the mean and maximum ATE using the ground truth data with *evo*<sup>6</sup>.

The results listed in Table II demonstrate that our approach reduces the mean ATE by more than half compared to the next best method. Furthermore, our method achieves a mean ATE that is a magnitude lower than the LiDAR odometry approach. Figure 4 shows that our method accumulates no drift over the traversed distance. Notably, we observe an unusually high deviation in a specific section compared to the rest of the trajectory. Figure 4 (I) and (II) show the point cloud generated from the ground truth data and our approach for this section. We identify significant deviations in the provided "ground truth" data for the two passes of the section, particularly with vertical offsets exceeding 1 m in some regions. Hence, the ground truth provided by KITTI cannot be regarded as accurate values, affecting the overall evaluation and the metrics presented.

Beyond the KITTI dataset, we demonstrate similar performance for the NCLT and EDGAR datasets, where our method exhibits no drift over time. On the EDGAR dataset, again the largest ATEs occur in the section with bad GNSS signals, most likely due to the signal blockage caused by underpasses and tall building walls (Figure 5). For NCLT, although deviations are the largest, our pose estimation remains robust despite the challenging dynamics and even across an unmapped indoor section (Figure 6).

<sup>6</sup><https://github.com/MichaelGrupp/evo>

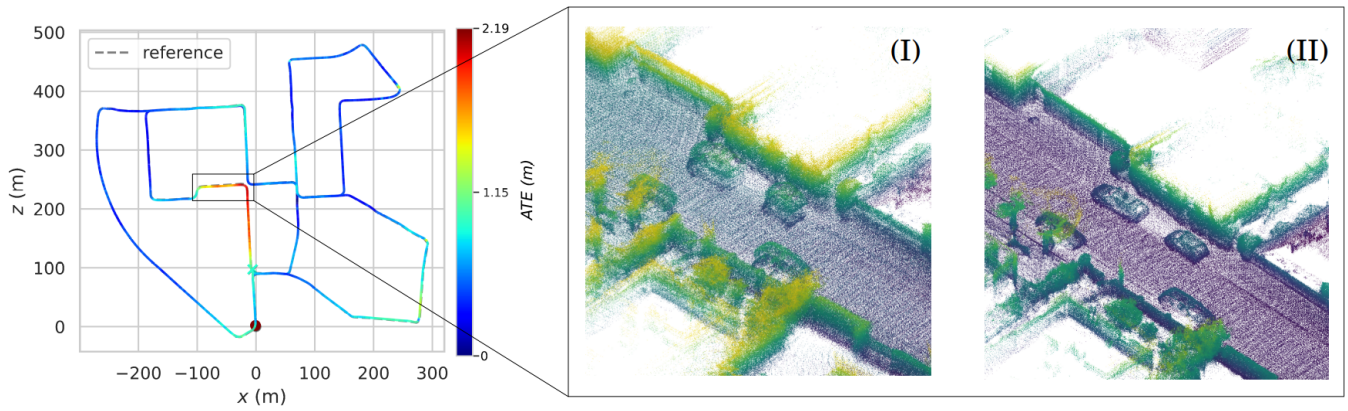


Fig. 4: Absolute Trajectory Error (ATE) of our approach for KITTI Seq. 00. (I) Point cloud created from the "ground truth" data. (II) Point cloud created with our approach.

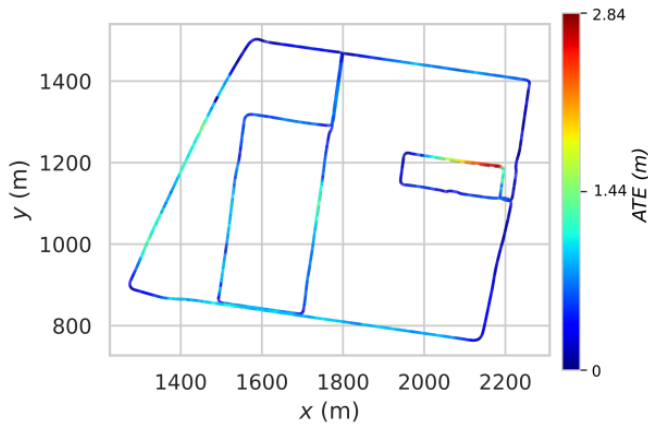


Fig. 5: Absolute Trajectory Error (ATE) of our approach for the EDGAR Campus dataset.

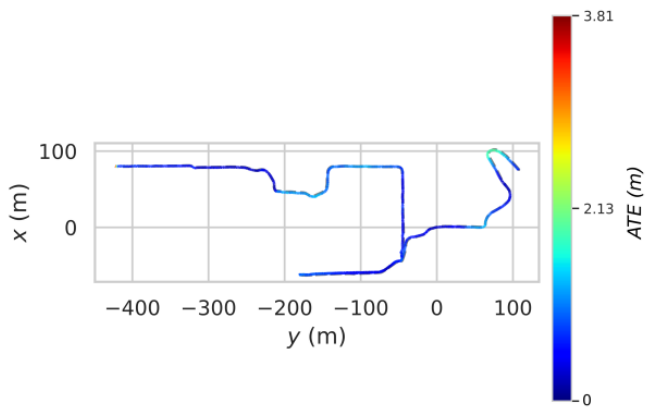


Fig. 6: Absolute Trajectory Error (ATE) of our approach for the NCLT 2013-01-1 dataset.



Fig. 7: KITTI Seq. 00 point cloud map, created with our approach, plotted to the orthophoto of Karlsruhe.

We obtain a global pose directly from our approach and only transform it into a local coordinate system for evaluation. On Figure 7, we show the overload of the directly generated map by our approach on georeferenced orthophotos of Karlsruhe<sup>2</sup>.

In addition to the ATE, we also evaluated the RTE using the KITTI methodology (Table III). For the KITTI dataset, our approach is outperformed by the LiDAR odometry algorithm KISS-ICP. This result can be attributed to the high consistency and smooth trajectory generated by KISS-ICP, which minimizes drift over the short averaged segments used

TABLE II: Mean and max Absolute Trajectory Error (ATE) in [m] for the evaluated datasets. Bold represents the best results and underscores the second-best results.

Method	Reference	KITTI Seq. 00		NCLT 2013-01-1		EDGAR Campus	
		mean ↓	max ↓	mean ↓	max ↓	mean ↓	max ↓
RC-MVO	[18]	3.76	14.01	-	-	-	-
AWYLaI	[24]	2.0	12.0	-	-	-	-
LiDAR-OSM	[22]	1.37	3.34	-	-	-	-
OSM-SLAM	[23]	3.15	11.06	-	-	-	-
KISS-ICP	[1]	6.71	15.20	3.26	15.99	66.40	259.13
OpenLiDARMap	(ours)	<b>0.66</b>	<b>2.19</b>	<b>1.02</b>	<b>3.81</b>	<b>0.52</b>	<b>2.84</b>

in the KITTI metric. However, on the NCLT dataset, which features high dynamics and a challenging environment, our method demonstrates a better performance. Similarly, the advantages of our approach are evident on the EDGAR dataset, where we maintain consistent trajectories over long distances without drift, leading to lower relative errors.

To assess how well our approach performs compared to pure scan-to-map algorithms, we tried to evaluate the current state of the art on our sparse reference map. However, none of LiLoc [34], BM-Loc [35], HDL\_localization [11], DLL [36], FAST\_LIO\_LOCALIZATION<sup>7</sup>, and lidar\_localization\_ros2<sup>8</sup> was able to finish KITTI Seq. 00, leaving us without any results to compare.

### C. Local Consistency Evaluation

For quantitative evaluation of map consistency, we use the Mean Map Entropy (MME) metric [37]. Specifically, we compare the MME between the point cloud map generated by OpenLiDARMap and the map generated from the ground truth transformations of the individual scans.

To facilitate this comparison, we preprocess the point clouds by cropping them to a 100×100 m region and downsampling individual clouds to a voxel size of 0.25 m. Notably, the composite map remains unfiltered to avoid introducing bias into the evaluation. This preprocessing step is essential to manage the computational complexity caused by the size of the maps.

In the case of the KITTI dataset, we can also use the MME to show that the ground truth is not exact. Our map shows a better (lower) score compared to the ground truth (Table IV). The same can also be shown for the NCLT results, where our approach reaches a lower score than the map generated from the ground truth data. For the EDGAR dataset, the MME generated with the ground truth is lower than the results of our approach.

### D. Out-of-Date Reference Maps

Finally, we demonstrate that our method does not rely on up-to-date reference maps. Across all datasets, we show that neither current map data nor temporal alignment between the maps and the LiDAR frames is necessary. For instance, the surface data used in the KITTI dataset originates from 2000

to 2023, while the building data stems from 2023, and the evaluated dataset was collected in 2011. Similarly, the NCLT dataset’s data sources span from 2013 to 2024, whereas the EDGAR dataset spans from 2023 to 2024.

The accompanying Figure 8 and Figure 9 highlight discrepancies between the sparse maps and the datasets, such as missing buildings or structural differences. These variations emphasize the minimal requirements for input data in our approach. For instance, building outlines for the NCLT dataset were extracted from OSM data, whereas those for KITTI and EDGAR were derived from spatial building models. Moreover, the resolution and type of input data vary significantly: KITTI and NCLT datasets rely on 1 m-resolution GeoTIFFs, while the EDGAR dataset benefits from raw LiDAR point clouds obtained through aerial scans. This diversity highlights the adaptability of our method to sparse maps with significantly different compositions.

As a final note, our approach focuses on mapping, making runtime not a concern for us. Despite that, we are able to run the entire pipeline in about 30 ms per KITTI frame on a modern PC with an AMD Ryzen 7700.

## V. LIMITATIONS AND FUTURE WORK

Unlike the ATE analysis, where our approach showed clear improvements, the RTE analysis yielded less conclusive results. This result can be primarily attributed to rotational errors, which have a particularly strong impact on the KITTI metric. Future work could address this limitation by improving the initial estimation, such as using homogeneous transforms or incorporating the time differences between frames.

A key requirement for the functionality of our approach is the availability of a digital surface model. While such data is available for large parts of the world, it is not universally accessible. A notable example is South Korea, where the lack of digital surface models prevents us from evaluating our approach on widely used datasets such as MulRan [38] or HeLiPR [39].

Due to the simple ICP-based scan-to-scan matching strategy, our method is limited in handling unmapped regions, such as long tunnels or extensive indoor areas. However, the modular design of our approach allows for future integration of more advanced LiDAR Odometry algorithms to address these challenges. Additionally, significant environ-

<sup>7</sup>[https://github.com/HViktorTsoi/fast\\_lio\\_localization](https://github.com/HViktorTsoi/fast_lio_localization)

<sup>8</sup>[https://github.com/rsasaki0109/lidar\\_localization\\_ros2](https://github.com/rsasaki0109/lidar_localization_ros2)



TABLE III: Relative Trajectory Error (RTE) using the KITTI methodology for the evaluated datasets.

Method	Reference	KITTI Seq. 00		NCLT 2013-01-1		EDGAR Campus	
		trans. ↓ [%]	rot. ↓ [deg/m]	trans. ↓ [%]	rot. ↓ [deg/m]	trans. ↓ [%]	rot. ↓ [deg/m]
KISS-ICP	[1]	<b>0.51</b>	<b>0.0017</b>	2.31	0.0161	2.77	0.0095
OpenLiDARMap	(ours)	0.53	0.0025	<b>1.93</b>	<b>0.0116</b>	<b>1.44</b>	<b>0.0046</b>

TABLE IV: Mean Map Entropy for the frames transformed with the ground truth data and OpenLiDARMap results. Lower ↓ is better.

Method	KITTI Seq. 00	NCLT 2013-01-1	EDGAR Campus
Ground Truth	-6.293	-6.212	<b>-6.317</b>
OpenLiDARMap (ours)	<b>-6.448</b>	<b>-6.339</b>	-6.231

mental changes can lead to erroneous results, emphasizing the need for further investigations across diverse scenarios to evaluate robustness under varying conditions.

## VI. CONCLUSIONS

In this paper, we presented an approach for georeferenced point cloud mapping that operates without the need for GNSS. By combining a scan-to-map and scan-to-scan point cloud registration method within an optimization framework, we achieved accurate mapping across diverse environments, vehicles, and LiDAR setups. Our experiments suggest that the proposed method effectively eliminates drift over long distances and is robust to variations in environmental conditions and sensor configurations. Our experiments suggest that the proposed method enables accurate georeferenced point cloud mapping without relying on GNSS sensors.

## ACKNOWLEDGEMENTS

The research was partially funded by the Bavarian Research Foundation (BFS) and through basic research funds of the Institute of Automotive Technology (FTM). Anonymized for Review Version

## REFERENCES

- [1] I. Vizzo, T. Guadagnino, B. Mersch, L. Wiesmann, J. Behley, and C. Stachniss, “Kiss-icp: In defense of point-to-point icp – simple, accurate, and robust registration if done the right way,” *IEEE Robotics and Automation Letters*, vol. 8, pp. 1029–1036, 2 2023.
- [2] X. Zheng and J. Zhu, “Traj-lio: In defense of lidar-only odometry using an effective continuous-time trajectory,” *IEEE Robotics and Automation Letters*, vol. 9, pp. 1961–1968, 2 2024.
- [3] C. Bai, T. Xiao, Y. Chen, H. Wang, F. Zhang, and X. Gao, “Faster-lio: Lightweight tightly coupled lidar-inertial odometry using parallel sparse incremental voxels,” *IEEE Robotics and Automation Letters*, vol. 7, pp. 4861–4868, 4 2022.
- [4] W. Xu, Y. Cai, D. He, J. Lin, and F. Zhang, “Fast-lio2: Fast direct lidar-inertial odometry,” *IEEE Transactions on Robotics*, vol. 38, pp. 2053–2073, 8 2022.
- [5] X. Zheng and J. Zhu, “Traj-lio: A resilient multi-lidar multi-imu state estimator through sparse gaussian process,” 2024.

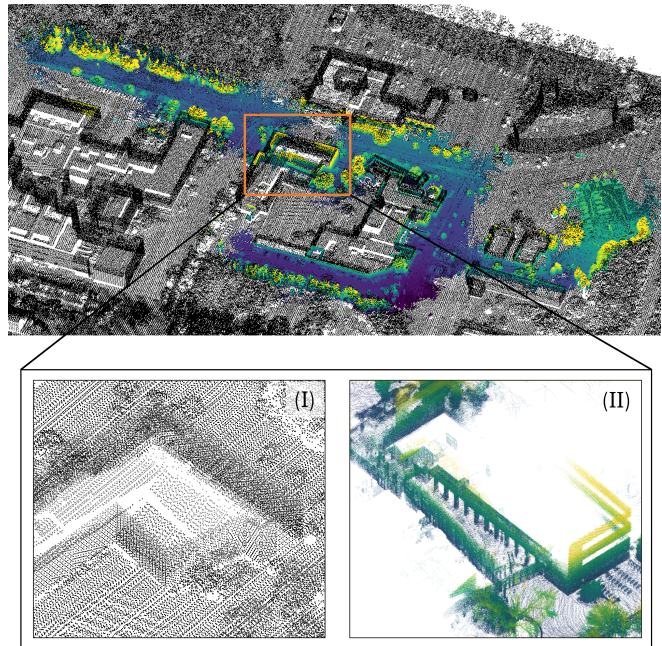


Fig. 8: Overload of the sparse reference map and the final point cloud map created with our approach for the NCLT 2013-01-1 dataset. (I) shows part of the reference map, and (II) shows the point cloud map generated with our approach for an indoor section of the dataset that we were able to map despite the missing correspondences between the onboard LiDAR frames and the reference map.

- [6] P. Dellenbach, J.-E. Deschaud, B. Jacquet, and F. Goulette, “Ct-icp: Real-time elastic lidar odometry with loop closure,” in *2022 International Conference on Robotics and Automation (ICRA)*. IEEE, 5 2022, pp. 5580–5586.
- [7] D. Yifan, X. Zhang, Y. Li, G. You, X. Chu, J. Ji, and Y. Zhang, “Cellmap: Enhancing lidar slam through elastic and lightweight spherical map representation,” 2024.
- [8] K. Koide, M. Yokozuka, S. Oishi, and A. Banno, “Glim: 3d range-inertial localization and mapping with gpu-accelerated scan matching factors,” *Robotics and Autonomous Systems*, vol. 179, p. 104750, 9 2024.
- [9] Y. Pan, X. Zhong, L. Wiesmann, T. Posewsky, J. Behley, and C. Stachniss, “Pin-slam: Lidar slam using a point-based implicit neural representation for achieving global map consistency,” *IEEE Transactions on Robotics*, vol. 40, pp. 4045–4064, 2024.
- [10] J. Jeong, J. Y. Yoon, H. Lee, H. Darweesh, and W. Sung, “Tutorial on high-definition map generation for automated driving in urban environments,” *Sensors*, vol. 22, p. 7056, 9 2022.
- [11] K. Koide, J. Miura, and E. Menegatti, “A portable three-dimensional lidar-based system for long-term and wide-area people behavior measurement,” *International Journal of Advanced Robotic Systems*, vol. 16, 3 2019.
- [12] K. Koide, S. Oishi, M. Yokozuka, and A. Banno, “Tightly coupled range inertial localization on a 3d prior map based on sliding window

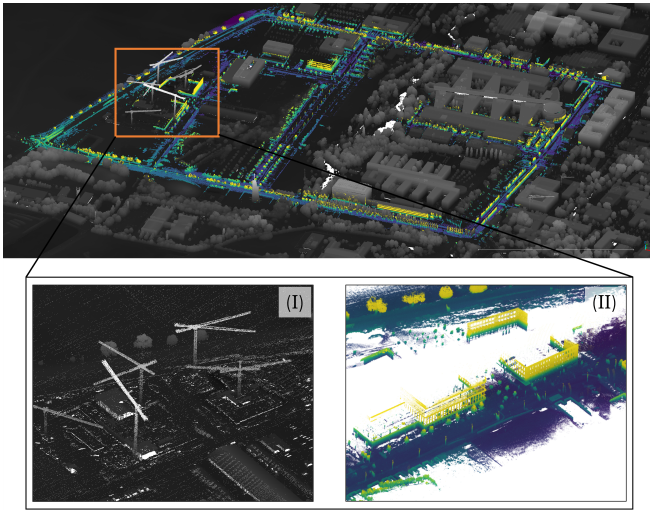


Fig. 9: Overload of the sparse reference map and the final point cloud map created with our approach for the EDGAR Campus dataset. Highlighted is a part of the map that still shows (I) the start of construction with multiple cranes in the reference map, while (II) the generated map from the LiDAR frames shows the completed building facades.

- factor graph optimization,” in *2024 IEEE International Conference on Robotics and Automation (ICRA)*. IEEE, 5 2024, pp. 1745–1751.
- [13] M. Leitenstern, F. Sauerbeck, D. Kulmer, and J. Betz, “Flexmap fusion: Georeferencing and automated conflation of hd maps with openstreetmap,” 2024.
- [14] A. Cramariuc, L. Bernreiter, F. Tschopp, M. Fehr, V. Reijgwart, J. Nieto, R. Siegwart, and C. Cadena, “maplab 2.0 – a modular and multi-modal mapping framework,” *IEEE Robotics and Automation Letters*, vol. 8, pp. 520–527, 2 2023.
- [15] F. Dellaert, “borglab/gtsam,” 2022, <https://github.com/borglab/gtsam>, 10.5281/zenodo.5794541.
- [16] G. Floros, B. van der Zander, and B. Leibe, “Openstreetslam: Global vehicle localization using openstreetmaps,” in *2013 IEEE International Conference on Robotics and Automation*. IEEE, 5 2013, pp. 1054–1059.
- [17] B. Suger and W. Burgard, “Global outer-urban navigation with openstreetmap,” in *2017 IEEE International Conference on Robotics and Automation (ICRA)*. IEEE, 5 2017, pp. 1417–1422.
- [18] S. Yang, R. Jiang, H. Wang, and S. S. Ge, “Road constrained monocular visual localization using gaussian-gaussian cloud model,” *IEEE Transactions on Intelligent Transportation Systems*, vol. 18, pp. 3449–3456, 12 2017.
- [19] F. Yan, O. Vysotska, and C. Stachniss, “Global localization on openstreetmap using 4-bit semantic descriptors,” in *2019 European Conference on Mobile Robots (ECMR)*. IEEE, 9 2019, pp. 1–7.
- [20] A. L. Ballardini, S. Fontana, D. Cattaneo, M. Matteucci, and D. G. Sorrenti, “Vehicle localization using 3d building models and point cloud matching,” *Sensors*, vol. 21, p. 5356, 8 2021.
- [21] Y. Cho, G. Kim, S. Lee, and J.-H. Ryu, “Openstreetmap-based lidar global localization in urban environment without a prior lidar map,” *IEEE Robotics and Automation Letters*, vol. 7, pp. 4999–5006, 4 2022.
- [22] M. Elhousni, Z. Zhang, and X. Huang, “Lidar-osm-based vehicle localization in gps-denied environments by using constrained particle filter,” *Sensors*, vol. 22, p. 5206, 7 2022.
- [23] M. Frosi, V. Gobbi, and M. Matteucci, “Osm-slam: Aiding slam with openstreetmaps priors,” *Frontiers in Robotics and AI*, vol. 10, 3 2023.
- [24] I. D. Miller, A. Cowley, R. Konkimalla, S. S. Shivakumar, T. Nguyen, T. Smith, C. J. Taylor, and V. Kumar, “Any way you look at it: Semantic crossview localization and mapping with lidar,” *IEEE Robotics and Automation Letters*, vol. 6, pp. 2397–2404, 4 2021.
- [25] Z. Xia, Y. Shi, H. Li, and J. F. P. Kooij, *Adapting Fine-Grained Cross-View Localization to Areas Without Fine Ground Truth*, 2024, pp. 397–415.
- [26] K. Koide, “small\_gicp: Efficient and parallel algorithms for point cloud registration,” *Journal of Open Source Software*, vol. 9, p. 6948, 8 2024.
- [27] S. Agarwal and K. Mierle, “Ceres solver,” 2023, <https://github.com/ceres-solver/ceres-solver>.
- [28] A. Geiger, P. Lenz, and R. Urtasun, “Are we ready for autonomous driving? the kitti vision benchmark suite,” in *2012 IEEE Conference on Computer Vision and Pattern Recognition*. IEEE, 6 2012, pp. 3354–3361.
- [29] A. Geiger, P. Lenz, C. Stiller, and R. Urtasun, “Vision meets robotics: The kitti dataset,” *The International Journal of Robotics Research*, vol. 32, pp. 1231–1237, 9 2013.
- [30] N. Carlevaris-Bianco, A. K. Ushani, and R. M. Eustice, “University of michigan north campus long-term vision and lidar dataset,” *The International Journal of Robotics Research*, vol. 35, pp. 1023–1035, 8 2016.
- [31] J.-E. Deschaud, “Imls-slam: Scan-to-model matching based on 3d data,” in *2018 IEEE International Conference on Robotics and Automation (ICRA)*. IEEE, 5 2018, pp. 2480–2485.
- [32] P. Karle, T. Betz, M. Bosk, F. Fent, N. Gehrke, M. Geisslinger, L. Gressenbuch, P. Hafemann, S. Huber, M. Hübner, S. Huch, G. Kaljavesi, T. Kerbl, D. Kulmer, S. Maierhofer, T. Mascetta, F. Pfab, F. Rezabek, E. Rivera, S. Sagmeister, L. Seidlitz, F. Sauerbeck, I. Tahiraj, R. Trauth, N. Uhlemann, G. Würsching, B. Zarrouki, M. Althoff, J. Betz, K. Bengler, G. Carle, F. Diermeyer, J. Ott, and M. Lienkamp, “Edgar: An autonomous driving research platform – from feature development to real-world application,” 2023.
- [33] D. Kulmer, I. Tahiraj, A. Chumak, and M. Lienkamp, “Multi-lica: A motion- and targetless multi - lidar-to-lidar calibration framework,” in *2024 IEEE International Conference on Multisensor Fusion and Integration for Intelligent Systems (MFI)*. IEEE, 9 2024, pp. 1–7.
- [34] Y. Fang, Y. Li, K. Qian, F. Tombari, Y. Wang, and G. H. Lee, “Liloc: Lifelong localization using adaptive submap joining and egocentric factor graph,” 2024.
- [35] Y. Feng, Z. Jiang, Y. Shi, Y. Feng, X. Chen, H. Zhao, and G. Zhou, “Block-map-based localization in large-scale environment,” in *2024 IEEE International Conference on Robotics and Automation (ICRA)*. IEEE, 5 2024, pp. 1709–1715.
- [36] F. Caballero and L. Merino, “Dil: Direct lidar localization. a map-based localization approach for aerial robots,” in *2021 IEEE/RSJ International Conference on Intelligent Robots and Systems (IROS)*. IEEE, 9 2021, pp. 5491–5498.
- [37] J. Razlaw, D. Droschel, D. Holz, and S. Behnke, “Evaluation of registration methods for sparse 3d laser scans,” in *2015 European Conference on Mobile Robots (ECMR)*. IEEE, 9 2015, pp. 1–7.
- [38] G. Kim, Y. S. Park, Y. Cho, J. Jeong, and A. Kim, “Mulran: Multimodal range dataset for urban place recognition,” in *2020 IEEE International Conference on Robotics and Automation (ICRA)*. IEEE, 5 2020, pp. 6246–6253.
- [39] M. Jung, W. Yang, D. Lee, H. Gil, G. Kim, and A. Kim, “Helipr: Heterogeneous lidar dataset for inter-lidar place recognition under spatiotemporal variations,” *The International Journal of Robotics Research*, vol. 43, pp. 1867–1883, 10 2024.